LAMOST J1010+2358 IS NOT A PAIR-INSTABILITY SUPERNOVA RELIC

PIERRE N. THIBODEAUX © ^{1,2}, ALEXANDER P. JI © ^{1,2,3}, WILLIAM CERNY © ⁴, EVAN N. KIRBY © ⁵, AND JOSHUA D. SIMON ⁶

¹Department of Astronomy & Astrophysics, University of Chicago, 5640 S Ellis Avenue, Chicago, IL 60637, USA

²Kavli Institute for Cosmological Physics, University of Chicago, Chicago, IL 60637, USA

³Joint Institute for Nuclear Astrophysics

⁴Department of Astronomy, Yale University, New Haven, CT 06520, USA

⁵Department of Physics, University of Notre Dame, IN 46556, USA and

⁶Observatories of the Carnegie Institution for Science, 813 Santa Barbara St., Pasadena, CA 91101, USA

Version August 9, 2024

ABSTRACT

The discovery of a star formed out of pair-instability supernova ejecta would have massive implications for the Population III star initial mass function and the existence of stars over $100~M_{\odot}$, but none have yet been found. Recently, the star LAMOST J1010+2358 was claimed to be a star that formed out of gas enriched by a pair-instability supernova. We present a non-LTE abundance analysis of a new high-resolution Keck/HIRES spectrum of J1010+2358. We determined the carbon and aluminum abundances needed to definitively distinguish between enrichment by a pair-instability and core-collapse supernova. Our new analysis demonstrates that J1010 + 2358 does not have the unique abundance pattern of a a pair-instability supernova, but was instead enriched by the ejecta of a low mass core-collapse supernova. Thus, there are still no known stars displaying unambiguous signatures of pair-instability supernovae.

Subject headings: stars: abundances – first stars, galaxies, reionization

1. INTRODUCTION

The first Population III stars in the universe are thought to have been extremely massive (Bromm et al. 2001; Hirano et al. 2014). The top-heavy initial mass function should easily populate the mass range of $140-260\,\mathrm{M}_\odot$, where stars are expected to explode as pair-instability supernovae (PISNe, e.g., Heger et al. 2003; Yoon et al. 2012; Nomoto et al. 2013). PISNe are expected to produce a unique abundance pattern with extremely strong odd-even ratios (Heger & Woosley 2002; Takahashi et al. 2018). Detecting even one star with a PISN signature would have important implications for the Population III initial mass function (e.g., Koutsouridou et al. 2024).

However, stars exhibiting a clear PISN signature have remained elusive. The first claimed PISN detection (Aoki et al. 2014) turned out to have an abundance pattern more consistent with a core-collapse supernova (e.g., Takahashi et al. 2018). One difficulty with finding PISNe is that they likely enrich stars to relatively high metallicities $[Fe/H] \sim -2.5$ or -2.0, so they may be missed in most surveys that primarily target stars with $[Fe/H] \lesssim -3$ (Karlsson et al. 2008). The PISN signatures are rapidly erased by any contamination (e.g., Ji et al. 2015), so the signature should be searched for in the presence of contamination by other supernovae (Salvadori et al. 2019; Aguado et al. 2023).

Recently, Xing et al. (2023) discovered that the metalpoor star LAMOST J1010+2358 (hereafter abbreviated J1010+2358) is a likely candidate that has preserved a PISN signature. They found the star has high metallicity ([Fe/H] = -2.4), low [Mg/Fe], and an extreme odd-even effect including non-detections of Na, Sc, Zn, Sr, and Ba. The derived abundance pattern is a clear match to a massive $(260\,\mathrm{M}_\odot)$ PISN. However, Jeena et al. $(2024, \mathrm{hereafter\ J24})$ and Koutsouridou et al. (2024) pointed out that the abundance pattern could also be consistent with a core-collapse supernova (CCSN). Key elements needed to strengthen the PISN claim include low abundances of carbon, aluminum, and potassium, which were not measured in the original analysis.

Here we present a new abundance analysis of J1010 \pm 2358 using a high signal-to-noise ratio Keck/HIRES spectrum covering an expanded wavelength range. In Section 2, we discuss the data and then explain our method of deriving elemental abundances for J1010 \pm 2358. In Section 3, we present the best fitting SN models to our abundances, and we compare our findings to Xing et al. (2023, hereafter X23) in Section 4. Contrary to their result, and consistent with the alternate interpretation proposed by J24, we find that J1010 \pm 2358 is best explained by a CCSN and not a PISN progenitor.

2. OBSERVATIONS AND ABUNDANCE ANALYSIS

2.1. Observations

We obtained a spectrum of J1010 + 2358 on 2024 January 18 using Keck/HIRES (Vogt et al. 1994) with its red cross-disperser. The exposure time was 8100s over 5 exposures with a 1".1 slit and 2x1 binning, resulting in a resolution of $R \sim 36000$. Data were reduced using MAKEE v6.41. We also observed a nearby telluric standard (HR 3601) to verify that the lines used in this analysis are unaffected by telluric absorption. The signal-to-noise (S/N) is 30 per 0.02 Å pixel at 3950 Å where the blue Al lines are located and 75 per 0.03 Å pixel at 7700 Å where

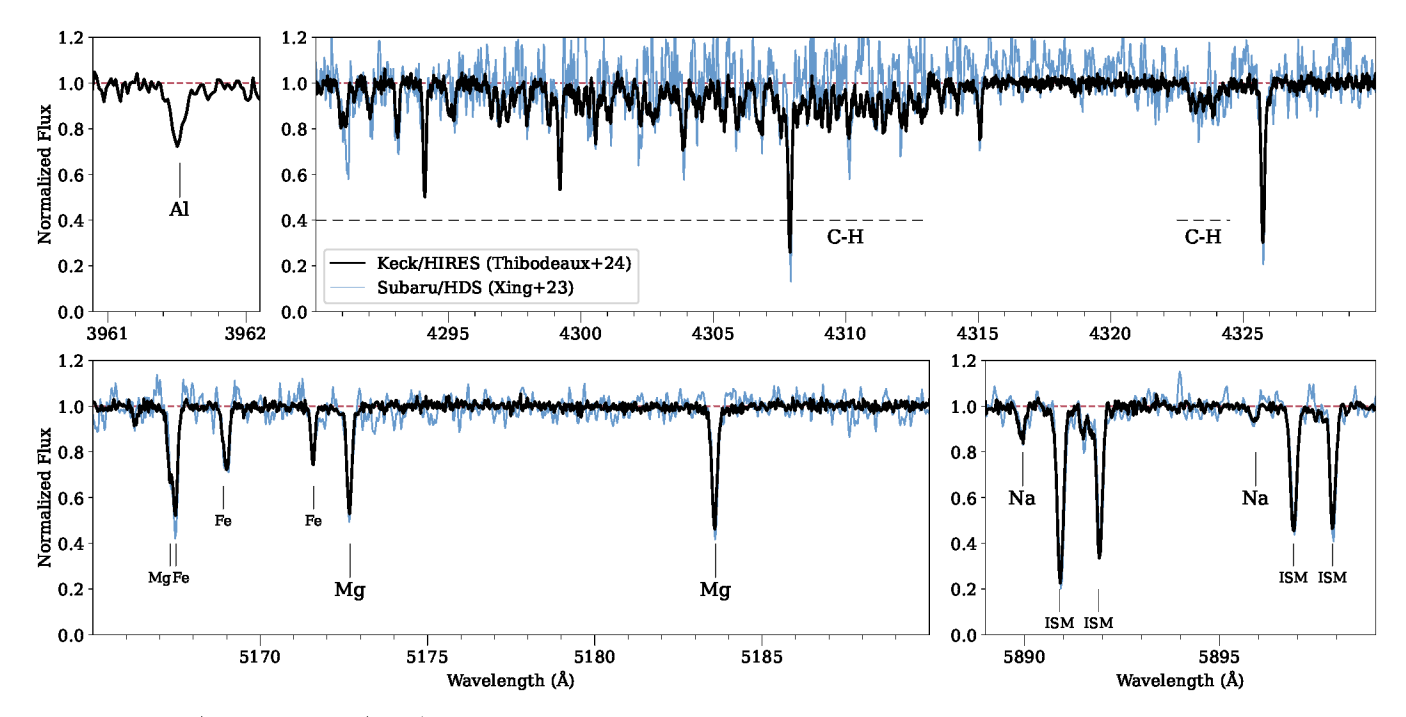


FIG. 1.— Keck/HIRES spectra (black) of J1010 + 2358 around aluminum, carbon, magnesium, and sodium features. Our re-reduction of X23's Subaru/HDS spectrum is plotted in blue for comparison, which shows clear Na D absorption. Our spectra are less noisy, allowing for the measurement of carbon. The HDS spectrum also lacks coverage of the aluminum lines.

TABLE 1 STELLAR ATMOSPHERE PARAMETERS

Parameter	X23	This work		
$T_{ m eff}$	$5860 \pm 120~\mathrm{K}$	$5700 \pm 200~\mathrm{K}$		
$\log g$	3.6 ± 0.2	4.68 ± 0.3		
v_t	$1.5 \pm 0.25 \mathrm{km} \mathrm{s}^{-1}$	$1.45 \pm 0.2 \mathrm{km s^{-1}}$		
[M/H]	-2.42	-2.5 ± 0.2		

NOTE: The stellar parameters we use for J1010 + 2358. Its primary difference from X23 is the log g value. The model metallicity [M/H] differs from the [Fe/H] fit from the spectrum.

the K 7699 Å line is located. We used smhr² (Casey 2014) to correct the radial velocity, normalize the echelle orders, and stitch the spectrum. Figure 1 shows portions of the spectrum around Al 3961 Å, the Na D lines, the Mg b lines, and CH G band. In contrast to X23, we clearly detect two Na D lines (see discussion in Section 4).

2.2. Stellar Parameters

We derived stellar parameters using Gaia DR3 photometry and astrometry (Gaia Collaboration et al. 2016; Brown et al. 2021). We dereddened the Gaia photometry using the Gaia DR3 relations³, and adopted color- $T_{\rm eff}$ relations from Mucciarelli et al. (2021). The surface gravity (log g) was determined using this $T_{\rm eff}$, applying bolometric corrections from Casagrande & VandenBerg (2018), and the distance from Bailer-Jones et al. (2018). To obtain the microturbulence v_t , we fixed the log g and $T_{\rm eff}$ and used ATLAS (Castelli & Kurucz 2004) with MOOG in smhr to balance the [Fe I/H] abundances with respect

to the reduced equivalent widths. Our adopted stellar parameters and uncertainties are compared in Table 1 to the values from X23.

To estimate an uncertainty on the parameters, we first looked at X23, who report $T_{\rm eff}=5860$ K, $\log g=3.6$, $[{\rm Fe/H}]=-2.42$, and $v_t=1.5$ km s⁻¹. However, the X23 value for $\log g$ (suggesting that J1010 + 2358 is a subgiant) is inconsistent with the $\log g$ required by the Gaia DR3 parallax (which implies J1010 + 2358 is a dwarf). Their reported temperature is consistent with the range of 5700-5900 K we found based on using different colors (all combinations of BP, G, RP, and K_s) of the Gaia photometry.

We also determined spectroscopic stellar parameters in two ways. First, we followed the method of Frebel et al. (2013), using excitation, ionization, and line strength balance and then applying a correction to the photometric temperature scale to determine $T_{\rm eff} = 5540$ K, $\log g = 4.20$, $\nu_t = 1.62$ km s⁻¹. Second, we determined stellar parameters including non-LTE (NLTE) effects using LOTUS (Li & Ezzeddine 2023). LOTUS uses pre-calculated curves of growth using the Fe model atom from Ezzeddine et al. (2016) to determine stellar parameters through excitation, ionization, and line strength balance (see Section 2.4 for more details). tained $T_{\rm eff}=5520\pm165$ K, $\log g=4.8\pm0.4,\ \nu_t=0.98\pm0.25$ km s⁻¹. Within the 0.3 dex uncertainty, the LOTUS NLTE $\log g$ is consistent with the $\log g$ from parallax, while the Frebel et al. (2013) $\log g$ is consistent when including an extra 0.3 dex offset (see Ezzeddine et al. 2020).

The effect of stellar parameter uncertainties on the final abundances is dominated by $T_{\rm eff}$, and we adopt a conservative uncertainty of ± 200 K to cover the range of values that we found. We adopt a log g uncertainty

² https://github.com/andycasey/smhr/tree/py38-mpl313

³ https://www.cosmos.esa.int/web/gaia/edr3-extinction-law

of 0.3 dex to include our range of log g values. Our v_t uncertainty is also 0.2 km s⁻¹, which is consistent with the Frebel et al. (2013) value and includes the upper end of the best-fit v_t range from LOTUS.

We adopted $[\alpha/\text{Fe}] = 0.0$ and a model metallicity [M/H] = -2.5 with an uncertainty of 0.2 dex because the ATLAS model atmosphere grid we used for $[\alpha/\text{Fe}] = 0.0$ does not extend below -2.5. While this value departs from our final [Fe/H] fit, the dependence of the model atmospheres on the [M/H] is weak and does not contribute strongly to our final abundance uncertainty.

2.3. LTE Abundances

We conducted an abundance analysis using a similar setup as X23: Castelli & Kurucz (2004) model atmospheres and MOOG radiative transfer that assumes local thermodynamic equilibrium (LTE) but includes scattering (Sneden 1973; Sobeck et al. 2011). Linelists for the analysis were adopted from Ji et al. (2020), with the atomic data originating from linemake (Placco et al. 2021). We fit equivalent widths and best-fit syntheses in smhr including formal 5σ upper limits for undetected lines (see Ji et al. 2020 for details).

We also used TSFitPy (Gerber et al. 2023), which uses Turbospectrum (Plez 2012) and the standard MARCS model atmospheres (Gustafsson et al. 2008) to fit selected lines with syntheses. The abundances derived via this method were consistent with the MOOG abundances for most lines, and we adopt line-by-line differences between MOOG/ATLAS and Turbospectrum/MARCS as systematic uncertainties for each line.

We calculated an abundance and an associated error for each detected line in our analysis. The total error $E_{i,\mathrm{tot}}$ for each line i was calculated as the quadrature sum of the statistical error of the MOOG fits, the abundance difference of the MOOG and TSFitPy fits, the abundance difference that comes from increasing one of T_{eff} , $\log g$, [M/H], and v_t by the adopted uncertainties, and a minimum systematic error of 0.1 dex for any unmodeled effects. The final LTE abundances are weighted means of the individual line abundances for each species, using inverse variance weights $w_i = 1/E_{i,\mathrm{tot}}^2$. The error on the abundance is the uncertainty of the weighted mean, $\sigma_{\epsilon} = (\sum_i w_i)^{-1/2}$. The uncertainty of the [X/Fe] ratios, σ_{XFe} , differ from σ_{ϵ} because they account for correlations in X and Fe due to the stellar parameter uncertainties.

2.4. NLTE Corrections

The assumption of local thermodynamic equilibrium (LTE) fixes the distribution of atoms across their energy levels according to the Saha-Boltzmann equation. However, radiative and collisional interactions can cause the level populations to deviate from LTE. These non-LTE (NLTE) effects can be calculated by solving for statistical equilibrium, which influences the abundances inferred from the spectrum.

We used TSFitPy to determine NLTE corrections for individual lines (Gerber et al. 2023). TSFitPy uses precomputed NLTE departure coefficient grids calculated from the following model atoms: Na (Larsen et al. 2022), Mg (Bergemann et al. 2017), Ca (Mashonkina et al. 2017; Semenova et al. 2020), Ti (Bergemann 2011), Mn (Bergemann et al. 2019), Fe (Bergemann et al. 2012a; Semenova

TABLE 2 CHEMICAL ABUNDANCES

ID	N	$\log \epsilon$	[X/H]	[X/Fe]	σ_{ϵ}	σ_{XFe}	$\Delta_{ m NLTE}$
CH	2	6.10	-2.46	+0.16	0.26	0.21	
ΟI	1	< 8.59	< -0.18	< +2.44	limit	limit	
Na I	2	2.25	-4.04	-1.42	0.13	0.08	-0.03
MgI	4	4.30	-3.25	-0.63	0.11	0.08	+0.02
Al I	2	2.70	-3.73	-1.11	0.20	0.15	+0.61
KI	1	< 2.93	< -2.21	< +0.41	limit	limit	
Ca I	4	3.33	-3.04	-0.42	0.08	0.08	+0.04
Sc II	2	-0.18	-3.25	-0.63	0.19	0.21	
Ti I	3	2.28	-2.66	-0.04	0.15	0.10	+0.20
Ti II	5	2.05	-2.89	-0.27	0.07	0.12	+0.15
VI	1	< 1.52	< -2.37	< +0.25	limit	limit	
V II	1	< 2.08	< -1.81	<+0.81	limit	limit	
$\operatorname{Cr}\operatorname{I}$	2	2.73	-3.01	-0.39	0.15	0.08	
Mn I	2	2.52	-3.00	-0.37	0.13	0.11	+0.23
Fe I	73	4.88	-2.62	0.00	0.02	0.02	+0.09
Fe II	6	4.78	-2.72	-0.10	0.07	0.16	+0.01
Co I	2	2.18	-2.77	-0.14	0.15	0.09	+0.16
Ni I	1	3.57	-2.67	-0.05	0.20	0.12	+0.36
Zn I	1	< 2.64	< -1.92	< +0.70	limit	limit	
Sr II	2	-1.19	-4.06	-1.44	0.13	0.16	+0.07
Ba II	1	< -1.52	< -3.70	< -1.08	$_{ m limit}$	limit	
Eu II	1	< -0.85	< -1.37	<+1.25	limit	limit	

NOTE: The Magg et al. (2022) solar abundances were used for normalization. NLTE corrections are already applied to the log e and other abundance values. [X/Fe] has an additional NLTE correction for [Fe/H] already applied. We use the species Fe I, Ti II, and V II for SN model fitting.

et al. 2020), Co (Bergemann et al. 2010; Yakovleva et al. 2020), Ni (Bergemann et al. 2021; Voronov et al. 2022), Sr (Bergemann et al. 2012b). The NLTE correction for a single line is computed by taking the difference of the NLTE abundance and the LTE abundance from fitting the spectrum with TSFitPy. The NLTE corrections for the Aluminum lines were calculated seperately from Nordlander & Lind (2017). The total NLTE correction uses the MOOG line weights.

Our final abundances for J1010+2358 are the weighted average M00G abundances with the weighted average TSFitPy NLTE correction. These final abundances are listed in Table 2 as $\log \epsilon$, [X/H], and [X/Fe] alongside their error and the NLTE corrections (which are already incorporated into the abundances). We adopt solar abundances from Magg et al. (2022), which are revised from Asplund et al. (2009).

The final abundances are plotted in Figure 2 as [X/Fe] in comparison to the original X23 abundances and the distribution of abundances for stars with $-3 < [{\rm Fe/H}] < -1.5$ from the SAGA database (Suda et al. 2008). We adjust the SAGA aluminum abundances by our adopted NLTE correction since they were mainly computed in LTE. Compared to the SAGA stars, J1010 + 2358 is low in magnesium, calcium, and barium. Additionally, we find that the star is low in sodium, scandium, titanium, and strontium, though not as low as X23 reported.

3. SN YIELD FITS

We compare our abundances to a grid of 16800 CCSN nucleosynthesis models (Heger & Woosley 2010) and 14 PISN models (Heger & Woosley 2002). We determine the best-fit model by minimizing the mean absolute devi-

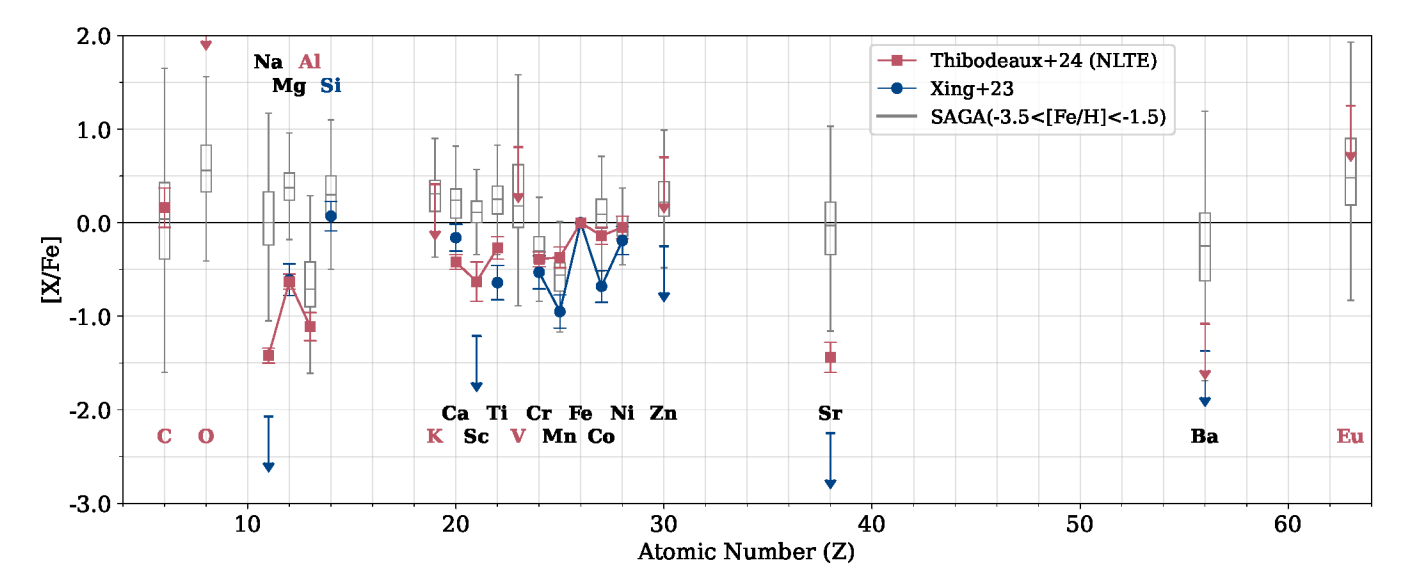


FIG. 2.— [X/Fe] values for J1010 + 2358 against those from X23 and against SAGA abundance ranges. The uncertainties on our abundances are $\sigma_{\rm X/Fe}$ from Table 2. The SAGA solar normalizations have been adjusted from Asplund et al. (2009) to Magg et al. (2022). We have applied our NLTE correction to the SAGA aluminum value. The colors of the element labels correspond to the elements only measured by us (red), only measured in X23 (blue), or in both (black).

ation between the abundances of J1010+2358 and those of the models for elements Z=6-30, allowing our [X/H] measurements to scale with a dilution parameter. Compared to a chi-squared (χ^2) minimization, this penalizes individual bad element fits less severely, though we still use the χ^2 to qualitatively visualize the range of well-fitting models. We reject any solutions that violate an upper limit, though this does not affect our final best fit.

We first verified that our SN fitting program worked by using the original X23 abundances to find the well-fitting (within 5σ) models from our grid, as shown in Figure 3(a). In this plot, we display models with a χ^2 value within 5σ of the optimal value. The best-fitting model is displayed in gold, whereas the well-fitting models are plotted in black, both in the Z vs. [X/H] plot and in the progenitor masses is also plotted in gray in the right plot. The reduced χ^2 is calculated as $\chi^2/(\text{d.o.f.})$, where the degrees of freedom is the number of elements fit (excluding upper limits) minus the number of model parameters (4 for CCSN, 2 for PISN).

With the X23 abundances, we recover their solution of a 260 M_{\odot} PISN model as the best-fitting solution but also found some CCSN models among the well-fitting models. These models are not within 4σ of the optimal χ^2 fit, so they are not preferred; however, it shows that a CCSN model could be found to explain their data. This possibility was first pointed out in J24, as was the fact that J1010+2358's low [Mg/Fe] does not preclude it from being enriched by a CCSN.

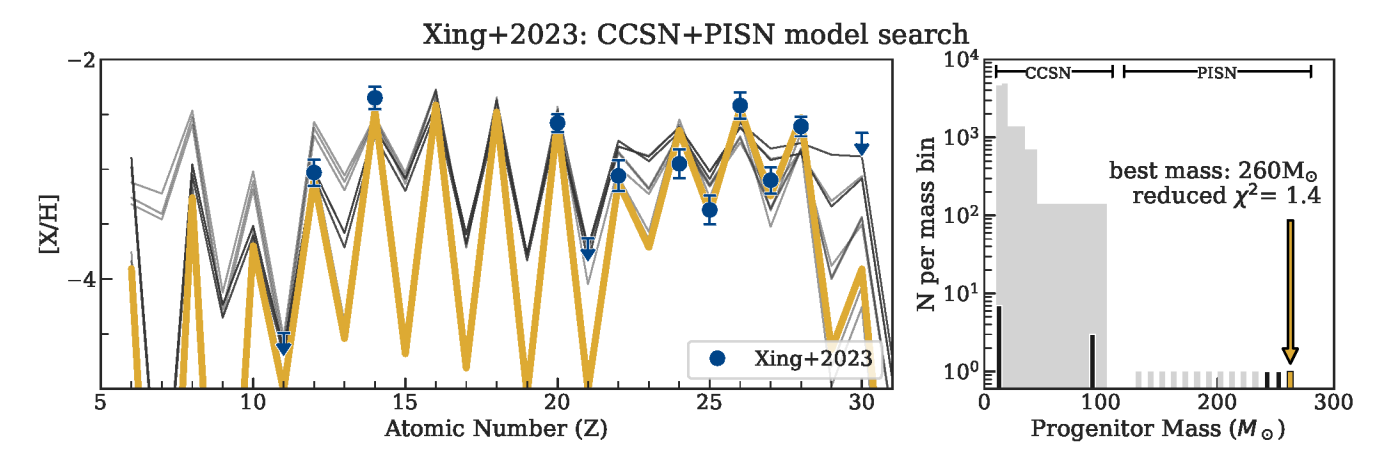
With our updated abundances, we find the best-fitting model (reduced $\chi^2 = 2.8$) to be an 11 M_{\odot} CCSN, as shown in Figure 3(b). As suggested by J24, the measurements of aluminum (Z=13) and carbon (Z=6) clearly distinguish between a CCSN and PISN. However, the rest of our abundances are consistent with a CCSN model as well, and we recover the same result when we remove carbon and aluminum from our fits. Even when excluding C

and Al, PISN models are completely excluded from the well-fitting models.

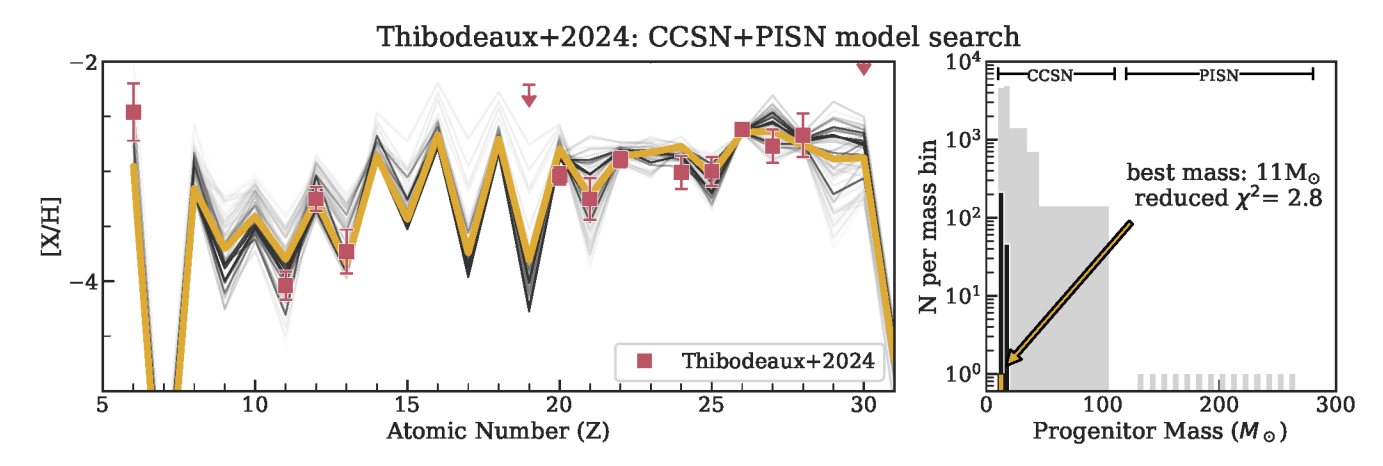
When we restrict our search to just PISN models, as displayed in Figure 3(c), the best-fitting model is a 220 M_{\odot} PISN. However, this is a lower-quality fit (reduced $\chi^2=28.8$). With the exception of sodium (Z=11) and magnesium (Z=12), we do not see a strong odd-even pattern in our measured abundances. The iron peak elements also lack the strong odd-even pattern that we would expect for a PISN. The difference in conclusions between our analysis and X23 stems from disagreements in the abundance measurements, most notably sodium, calcium (Z=20), scandium (Z=21), titanium (Z=25), and cobalt (Z=27).

Following X23, our conclusions are based on the PISN and CCSN model grids from Heger & Woosley (2002) and Heger & Woosley (2010). We note that we explored a much wider range of 1D metal-poor CCSN and PISN vield models described in Ji et al. (2024) (Limongi & Chieffi 2012, 2018; Nomoto et al. 2013; Grimmett et al. 2018; Ritter et al. 2018; Ebinger et al. 2020), finding identical conclusions. Most of these models assume spherical symmetry, zero metallicity, and no rotation. Such models are appropriate for PISNe (though see Yoon et al. 2012 for discussion of rotation), while the CCSN models are heavily parameterized with different explosion energies and mixing/fallback prescriptions. The impact of assuming 1D is harder to assess. While significant progress has been made in recent years on 3D CCSN simulations (e.g., Sieverding et al. 2020; Sieverding et al. 2023; Wang & Burrows 2023), they have all been run on solar metallicity progenitors. This said, existing 3D models suggest that nucleosynthesis effects are restricted to elements heavier than Ca $(Z \ge 20)$ (Sieverding et al. 2020). Even if we only consider elements with $\bar{Z} < 20$ and Fe, we would still conclude that PISNe are excluded while CCSNe are allowed.

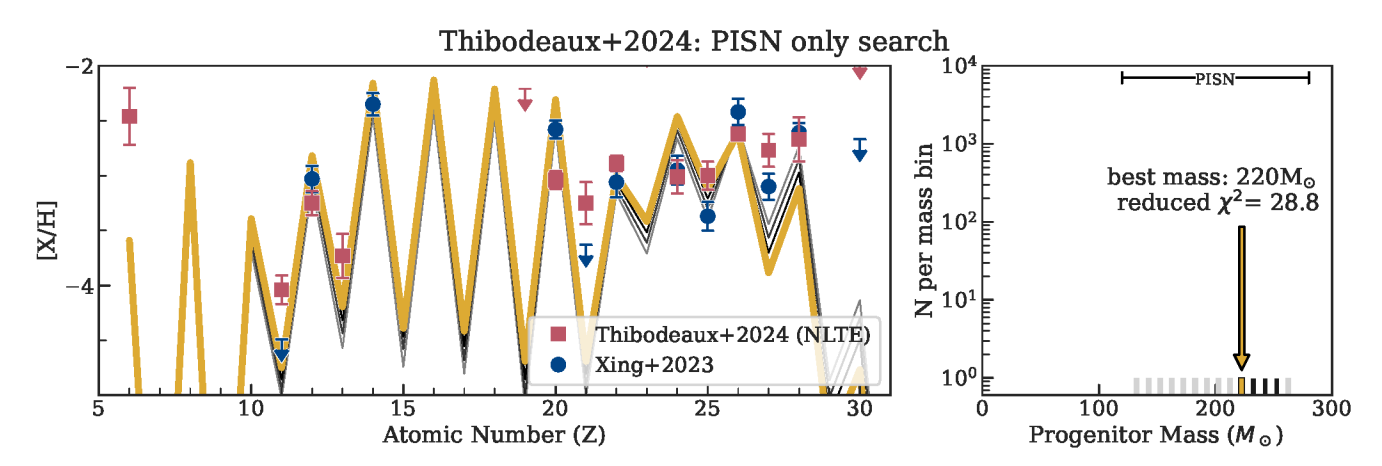
4. COMPARISON TO THE LITERATURE



(a) Our SN fitting of the abundances from X23. Their result of a $260M_{\odot}$ PISN is recovered as the best solution, though CCSN models are possible within 5σ of their measurements, as first noted by J24.



(b) The best-fitting model over all surveyed models is an 11 M_{\odot} CCSN model (Heger & Woosley 2010). The reduced chi-squared of this fit is 2.8, and the reduced chi-squareds of the other "well-fitting" models range between 2.2 and 6.4. PISNe are completely excluded.



(c) The best-fitting PISN model (Heger & Woosley 2002) compared to our abundances. The reduced χ^2 of this fit is 28.8, which is clearly a worse fit than the best CCSN model, especially for carbon (Z=6), sodium (Z=11), aluminum (Z=13), calcium (Z=20), scandium (Z=21), chromium (Z=24), and cobalt (Z=27).

Fig. 3.— Our model search. For the left plot in each subfigure, the best model (gold) is the one that minimizes the mean absolute error from the [X/H] abundances. This includes minimizing over a dilution parameter, which would shift the [X/H] of the model up or down. The uncertainties in these plots correspond to σ_{ϵ} in Table 2. The black "well-fitting" models are those whose χ^2 fall within a 5σ range of the minimum χ^2 value, and their opacities correspond to their strength-of-fit. Red squares correspond to the abundances found in this work, and the blue circles correspond to the abundances of X23. On the right of each subfigure, the progenitor masses of all the models are plotted as the grey histogram. The progenitor masses of the well-fitting models are plotted in black, and the best-fitting model is plotted in yellow.

Because it substantially affects the interpretation, we investigated possible reasons for our abundance differences compared to X23. First, they adopted different stellar parameters; most importantly, their $\log g$ of 3.6, differs from our value of 4.68. Though our spectroscopic and photometric parameters disagree with this result, we analyzed our spectrum with their stellar parameters and in LTE. The discrepancies between our values of scandium and magnesium are attributable to the different stellar parameters, but other elements remain inconsistent.

Our uncorrected, LTE abundances have a slightly stronger odd-even effect in the Fe peak elements; however, repeating our SN fitting procedure yielded the same result, with the same exclusion of PISNe from the well-fitting models. We could find no changes in the analysis of our spectrum that would reproduce the low Na or Si detection reported by X23.

In particular, our Na D detection is in direct conflict with the clear non-detection shown in their extended data figure 1. We thus downloaded the data used in X23 from the SMOKA archive (Baba et al. 2002) and reduced it in IRAF (Tody 1986, 1993; Fitzpatrick et al. 2024) with the HDS routines. The S/N of the HDS spectrum is lower than the HIRES spectrum, but we clearly see the two stellar Na D lines, as well as the stronger interstellar absorption components (Fig 1). The stellar Na lines are also visible on the raw 2D science image, where we identify some cosmic rays near the Na D lines. We suspect cosmic ray removal could have impacted the data reduction in X23. Furthermore, the 2D inspection shows that the star is not centered on the slit, making sky subtraction more difficult. As a final check, we measured equivalent widths of the lines we analyzed in our reduction of the HDS spectrum, finding no significant differences after accounting for spectrum noise. In any case, our higher S/N Keck/HIRES spectrum should provide a more reliable abundance analysis.

Recently, Skúladóttir et al. (2024) published an independent analysis of a VLT/UVES spectrum of J1010 + 2358. Their abundance measurements agree with our

analysis, and they additionally consider combinations of multiple supernova progenitors. Their work favors a combination of Population II and III CCSNe to explain the abundance pattern of $\rm J1010+2358$.

5. CONCLUSION

We present a new abundance analysis of the PISN candidate, J1010+2358. We collected a Keck/HIRES spectrum and calculated abundances using both equivalent width fitting and spectral synthesis fitting. Our new abundances confirm that the abundance pattern of J1010+2358 originated in a core-collapse supernova, and not a pair-instability supernova, as previously reported. Consistent with the suggestion of Jeena et al. (2024), our new carbon and aluminum measurements strongly favor a CCSN explanation over a PISN explanation. We find other discrepancies in our abundances compared with those determined by Xing et al. (2023). Our result means that a true PISN candidate is yet to be found.

ACKNOWLEDGMENTS

P.T. and A.P.J. acknowledge support by the National Science Foundation under grants AST-2206264 and AST-2307599. W.C acknowledges support from a Gruber Science Fellowship at Yale University. E.N.K. acknowledges support from NSF CAREER grant AST-2233781. This research has made use of the Keck Observatory Archive (KOA), which is operated by the W. M. Keck Observatory and the NASA Exoplanet Science Institute (NExScI), under contract with the National Aeronautics and Space Administration. Based in part on data collected at Subaru Telescope and obtained from the SMOKA, which is operated by the Astronomy Data Center, National Astronomical Observatory of Japan.

The authors wish to recognize and acknowledge the very significant cultural role and reverence that the summit of Maunakea has always had within the Native Hawaiian community. We are most fortunate to have the opportunity to conduct observations from this mountain.

REFERENCES

Aguado, D. S., Salvadori, S., Skúladóttir, Á., et al. 2023, MNRAS, 520, 866, doi: 10.1093/mnras/stad164
Aoki, W., Tominaga, N., Beers, T. C., Honda, S., & Lee, Y. S. 2014, Science, 345, 912, doi: 10.1126/science.1252633
Asplund, M., Grevesse, N., Sauval, A. J., & Scott, P. 2009, ARA&A, 47, 481, doi: 10.1146/annurev.astro.46.060407.145222
Baba, H., Yasuda, N., Ichikawa, S.-I., et al. 2002, Report of the National Astronomical Observatory of Japan, 6, 23
Bailer-Jones, C. A. L., Rybizki, J., Fouesneau, M., Mantelet, G., & Andrae, R. 2018, The Astronomical Journal, 156, 58, doi: 10.3847/1538-3881/aacb21
Bergemann, M. 2011, MNRAS, 413, 2184, doi: 10.1111/j.1365-2966.2011.18295.x
Bergemann, M., Collet, R., Amarsi, A. M., et al. 2017, ApJ, 847, 15, doi: 10.3847/1538-4357/aa88cb
Bergemann, M., Hansen, C. J., Bautista, M., & Ruchti, G. 2012a, A&A, 546, A90, doi: 10.1051/0004-6361/201219406
— 2012b, A&A, 546, A90, doi: 10.1051/0004-6361/201219406
Bergemann, M., Pickering, J. C., & Gehren, T. 2010, MNRAS, 401, 1334, doi: 10.1111/j.1365-2966.2009.15736.x
Bergemann, M., Gallagher, A. J., Eitner, P., et al. 2019, A&A, 631, A80, doi: 10.1051/0004-6361/201935811
Bergemann, M., Hoppe, R., Semenova, E., et al. 2021, MNRAS, 508, 2236, doi: 10.1093/mnras/stab2160
Bromm, V., Ferrara, A., Coppi, P. S., & Larson, R. B. 2001, MNRAS, 328, 969, doi: 10.1046/j.1365-8711.2001.04915.x

Brown, A. G., Vallenari, A., Prusti, T., et al. 2021, Astronomy and Astrophysics, 649, 1, doi: 10.1051/0004-6361/202039657
Casagrande, L., & VandenBerg, D. A. 2018, MNRAS, 479, L102, doi: 10.1093/mnras1/s1y104
Casey, A. R. 2014, ArXiv e-prints.
https://arxiv.org/abs/1405.5968
Castelli, F., & Kurucz, R. L. 2004, New Grids of ATLAS9 Model Atmospheres. https://arxiv.org/abs/astro-ph/0405087
Ebinger, K., Curtis, S., Ghosh, S., et al. 2020, ApJ, 888, 91, doi: 10.3847/1538-4357/ab5dcb
Ezzeddine, R., Merle, T., & Plez, B. 2016, Astronomische Nachrichten, 337, 850, doi: https://doi.org/10.1002/asna.201612384
Ezzeddine, R., Rasmussen, K., Frebel, A., et al. 2020, The Astrophysical Journal, 898, 150, doi: 10.3847/1538-4357/ab9d1a
Fitzpatrick, M., Placco, V., Bolton, A., et al. 2024, arXiv e-prints, arXiv:2401.01982, doi: 10.48550/arXiv.2401.01982
Frebel, A., Casey, A. R., Jacobson, H. R., & Yu, Q. 2013, ApJ, 769, 57, doi: 10.1088/0004-637X/769/1/57
Gaia Collaboration, Prusti, T., de Bruijne, J. H. J., et al. 2016, A&A, 595, A1, doi: 10.1051/0004-6361/201629272
Gerber, J. M., Magg, E., Plez, B., et al. 2023, A&A, 669, A43, doi: 10.1051/0004-6361/202243673
Grimmett, J. J., Heger, A., Karakas, A. I., & Müller, B. 2018, MNRAS, 479, 495, doi: 10.1093/mnras/sty1417
Gustafsson, B., Edvardsson, B., Eriksson, K., et al. 2008, A&A,

486, 951, doi: 10.1051/0004-6361:200809724

```
Heger, A., Fryer, C. L., Woosley, S. E., Langer, N., & Hartmann,
D. H. 2003, ApJ, 591, 288, doi: 10.1086/375341
Heger, A., & Woosley, S. E. 2002, ApJ, 567, 532,
doi: 10.1086/338487
```

—. 2010, ApJ, 724, 341, doi: 10.1088/0004-637X/724/1/341 Hirano, S., Hosokawa, T., Yoshida, N., et al. 2014, ApJ, 781, 60, doi: 10.1088/0004-637X/781/2/60

Jeena, S. K., Banerjee, P., & Heger, A. 2024, MNRAS, 527, 4790, doi: 10.1093/mnras/stad349

Ji, A. P., Frebel, A., & Bromm, V. 2015, MNRAS, 454, 659, doi: 10.1093/mnras/stv205

doi: 10.1095/mnras/stv2052 Ji, A. P., Li, T. S., Hansen, T. T., et al. 2020, AJ, 160, 181, doi: 10.3847/1538-3881/abacb6 Ji, A. P., Curtis, S., Storm, N., et al. 2024, ApJ, 961, L41, doi: 10.3847/2041-8213/ad19c4

Karlsson, T., Johnson, J. L., & Bromm, V. 2008, ApJ, 679, 6, doi: 10.1086/533520

Koutsouridou, I., Salvadori, S., & Skúladóttir, Á. 2024, The Astrophysical Journal Letters, 962, L26, doi: 10.3847/2041-8213/ad2466

Larsen, S. S., Eitner, P., Magg, E., et al. 2022, A&A, 660, A88, doi: 10.1051/0004-6361/202142243

Li, Y., & Ezzeddine, R. 2023, The Astronomical Journal, 165, 145, doi: 10.3847/1538-3881/acb7f0
Limongi, M., & Chieffi, A. 2012, ApJS, 199, 38,

doi: 10.1088/0067-0049/199/2/38 - 2018, ApJS, 237, 13, doi: 10.3847/1538-4365/aacb24

Magg, E., Bergemann, M., Serenelli, A., et al. 2022, A&A, 661, A140, doi: 10.1051/0004-6361/202142971

Mashonkina, L., Sitnova, T., & Belyaev, A. K. 2017, A&A, 605, A53, doi: 10.1051/0004-6361/2017312

Mucciarelli, A., Bellazzini, M., & Massari, D. 2021, A&A, 653,

A90, doi: 10.1051/0004-6361/202140979 Nomoto, K., Kobayashi, C., & Tominaga, N. 2013, ARA&A, 51, 457, doi: 10.1146/annurev-astro-082812-140956

Nordlander, T., & Lind, K. 2017, A&A, 607, A75,

doi: 10.1051/0004-6361/201730427

Placco, V. M., Sneden, C., Roederer, I. U., et al. 2021, linemake:
Line list generator, Astrophysics Source Code Library, record

asci:2104.027. http://ascl.net/2104.027 Plez, B. 2012, Turbospectrum: Code for spectral synthesis, Astrophysics Source Code Library, record ascl:1205.004.

http://ascl.net/1205.004
Ritter, C., Herwig, F., Jones, S., et al. 2018, MNRAS, 480, 538, doi: 10.1093/mnras/sty1729

This paper was built using the Open Journal of Astrophysics LATEX template. The OJA is a journal which provides fast and easy peer review for new papers in the Salvadori, S., Bonifacio, P., Caffau, E., et al. 2019, MNRAS, 487, 4261, doi: 10.1093/mnras

7507, doi: 10.1007/militas/55221404 Semenova, E., Bergemann, M., Deal, M., et al. 2020, A&A, 643, A164, doi: 10.1051/0004-6361/202038833

Sieverding, A., Kresse, D., & Janka, H.-T. 2023, arXiv e-prints, arXiv:2308.09659, doi: 10.48550/arXiv.2308.0965

Sieverding, A., Müller, B., & Qian, Y.-Z. 2020, The Astrophysical Journal, 904, 163, doi: 10.3847/1538-4357/abc61b

Skúladóttir, Á., Koutsouridou, I., Vanni, I., et al. 2024, The Astrophysical Journal Letters, 968, L23, doi: 10.3847/2041-8213/ad4b1a

Sneden, C. A. 1973, PhD thesis, The University of Texas at Austin.

Sobeck, J. S., Kraft, R. P., Sneden, C., et al. 2011, AJ, 141, 175, doi: 10.1088/0004-6256/141/6/175
Suda, T., Katsuta, Y., Yamada, S., et al. 2008, PASJ, 60, 1159,

doi: 10.1093/pasj/60.5.1159 Takahashi, K., Yoshida, T., & Umeda, H. 2018, ApJ, 857, 111,

doi: 10.3847/1538-4357/aab95f

Tody, D. 1986, in Society of Photo-Optical Instrumentation Engineers (SPIE) Conference Series, Vol. 627, Instrumentation in astronomy VI, ed. D. L. Crawford, 733, doi: 10.1117/12.968154

Tody, D. 1993, in Astronomical Society of the Pacific Conference Series, Vol. 52, Astronomical Data Analysis Software and Systems II, ed. R. J. Hanisch, R. J. V. Brissenden, & J. Barnes,

Vogt, S. S., Allen, S. L., Bigelow, B. C., et al. 1994, in Society of Photo-Optical Instrumentation Engineers (SPIE) Conference Series, Vol. 2198, Instrumentation in Astronomy VIII, ed. D. L.

Crawford & E. R. Craine, 362, doi: 10.1117/12.176725 Voronov, Y. V., Yakovleva, S. A., & Belyaev, A. K. 2022, ApJ, 926, 173, doi: 10.3847/1538-4357/ac46fd

Wang, T., & Burrows, A. 2023, ApJ, 954, 114, doi: 10.3847/1538-4357/ace7b2

Xing, Q.-F., Zhao, G., Liu, Z.-W., et al. 2023, Nature, 618, 712,

Yakovleva, S. A., Belyaev, A. K., & Bergemann, M. 2020, Atoms, 8, doi: 10.3390/atoms8030034

Yoon, S. C., Dierks, A., & Langer, N. 2012, A&A, 542, A113, doi: 10.1051/0004-6361/201117769

astro-ph section of the arXiv, making the reviewing process simpler for authors and referees alike. Learn more at http://astro.theoj.org.